JOURNAL OF GEOPHYSICAL RESEARCH: OCEANS, VOL. 118, 5280–5295, doi:10.1002/jgrc.20358, 2013

Alongshore momentum balance analysis on a cuspate foreland

Nirnimesh Kumar,[1] George Voulgaris,[1] Jeffrey H. List,[2] and John C. Warner[2]

Received 11 January 2013; revised 7 August 2013; accepted 12 August 2013; published 15 October 2013.

[1] Nearshore measurements of waves and currents off Cape Hatteras, North Carolina, U.S.A, are used to investigate depth-averaged subtidal circulation and alongshore momentum balances in the surf and inner shelf region around a cuspate foreland. Data were collected on both sides of the cape representing shorefaces with contrasting shoreline orientation (north-south vs. northwest-southeast) subjected to the same wind forcing. In the nearshore, the subtidal flow is aligned with the local coastline orientation while at the cape point the flow is along the existing submerged shoal, suggesting that cape associated shoals may act as an extension of the coastline. Alongshore momentum balance analysis incorporating wave-current interaction by including vortex and Stokes-Coriolis forces reveals that in deep waters surface and bottom stress are almost in balance. In shallower waters, the balance is complex as nonlinear advection and vortex force become important. Furthermore, linearized momentum balance analysis suggests that the vortex force can be of the same order as wind and wave forcing. Farther southwest of Cape Hatteras point, wind and wave forcing alone fail to fully explain subtidal flow variability and it is shown that alongshore pressure gradient as a response to the wind forcing can close the momentum balance. Adjacent tide gauge data suggest that the magnitude of pressure gradient depends on the relative orientation of local coastline to the wind vector, and in a depth-averaged sense the pressure gradient generation due to change in coastline orientation even at km length scale is analogous to the effect of alongshore variable winds on a straight coastline.

Citation: Kumar, N., G. Voulgaris, J. H. List, and J. C. Warner (2013), Alongshore momentum balance analysis on a cuspate foreland, *J. Geophys. Res. Oceans*, *118*, 5280–5295, doi:10.1002/jgrc.20358.

1. Introduction

[2] Subtidal, wind driven circulation has been the subject of numerous experimental studies conducted at different nearshore environments along the US coast that include: the Middle Atlantic Bight (MAB) [e.g., *Feddersen et al*., 1998; *Lentz et al*., 1999; *Lentz*, 2001]; the inner and mid-shelf in Northern and Southern California [*Lentz*, 1994; *Lentz and Winant*, 1986]; Central Oregon Coast [*Kirincich and Barth*, 2009]; the South Atlantic Bight (SAB) [*Gutierrez et al*., 2005]; and Martha's Vineyard [*Fewings and Lentz*, 2010]. These studies have enhanced our understanding of wind-driven circulation and have identified the most important constituents of the momentum balance equation [see *Lentz and Fewings*, 2012 for a detailed review].

[3] It is only recently [*Lentz*, 2008; *Fewings and Lentz*, 2010] that the role of the Stokes-Coriolis force term [*Hasselmann*, 1970] has been considered in studies of shelf circulation. Vortex force (hereinafter referred to as VF) is another wave-related term [*Craik and Leibovich*, 1976] that represents the interaction between wave-induced mass drift and mean flow vorticity. Although no direct experimental data exist, results from recent modeling studies [*Uchiyama et al*., 2010; *Kumar et al*., 2012] have shown that nonlinear advection and VF can be dominant in the nearshore and especially within the surf zone. The contribution of these terms is expected to be more pronounced in regions with complex bathymetric features such as barred beaches and shallow regions with shoals present. Further, the role of VF also becomes important in areas with strong horizontal shear in cross/alongshelf velocity.

[4] Studies of flows around complex coastline configurations such as those found on capes [i.e., *McNinch and Luettich*, 2000] or over bathymetric features [i.e., *Sanay et al*., 2007] are limited mainly to tidal time scales. *Roughan et al*. [2005] and *Gan and Allen* [2002a, 2002b] presented work on wind-driven flows around capes focusing on upwelling dynamics in the leeward side of a cape, while *Barth et al*. [2005] studied transient wind driven circulation in a region with alongshelf topographic variations. Capes are characterized by abrupt changes in coastline orientation and a complex bathymetry and their role in subtidal circulation processes is not clear yet. In this contribution, experimental data from such a location are used to reveal some of the interactions between uneven coastline shape, waves and

[1]Marine Science Program, Department of Earth and Ocean Sciences, College of Arts and Sciences, University of South Carolina, Columbia, South Carolina, USA.
[2]U.S. Geological Survey, Coastal and Marine Geology Program, Woods Hole, Massachusetts, USA.

Corresponding author: N. Kumar, Marine Science Program, Department of Earth and Ocean Sciences, College of Arts and Sciences, University of South Carolina, Columbia, SC 29208, USA. (nkumar@geol.sc.edu)

2169-9275/13/10.1002/jgrc.20358

subtidal flow dynamics. The objectives of this work are to: (a) identify the subtidal circulation pattern in the inner shelf region around a cuspate foreland system with a complex morphology; (b) experimentally assess the role of VF and nonlinear advective acceleration terms in this subtidal circulation; and (c) reveal the response of the surf zone and inner shelf for a nonuniform coastline and complex bathymetry to surface waves and wind fields. In this contribution, we present estimates of VF and nonlinear acceleration terms from a combination of in situ data and a simplified momentum balance model, which are compared to wind stress and wave breaking induced acceleration.

[5] First we describe the study area and the data collection procedures in section 2. This is followed with an overview of the hydrodynamic conditions encountered in terms of wave activity and subtidal flows (section 3), while in section 4 the depth-averaged momentum balance is presented. The findings are discussed in section 5 while the final conclusions are presented in section 6.

Table 1. List of Instruments Deployed Around Cape Hatteras Point During February 2010

Site	Instrument Type[a]	Mean Water Depth (m)	Height Above Bed of First Bin (m)	Deployment Duration (Days)
N1	AQD	4.7	0.40	17
N2	AQD	7.0	0.40	17
N3	AQD	6.0	0.40	18
N4	ADCP	8.8	1.60	18
N5	ADCP	6.1	0.64	20
N6	AQD	4.7	0.40	20
O2	ADCP	10.7	0.64	45
O3	ADCP	10.0	0.64	45
N8	AQD	5.3	0.40	19
N9	ADCP	6.6	0.64	19
N11	AQD	5.0	0.40	20
N12	AQD	3.5	0.40	20
O1	ADCP	8.9	0.64	18

[a]AQD, Nortek aquadopp; ADCP, Teledyne RD Instruments acoustic Doppler current profiler.

2. Data Collection

[6] Inner shelf hydrodynamic data were collected over the period 3–22 February 2010 (Table 1) in the vicinity of Cape Hatteras, NC. The study site has a typical cape coastline configuration characterized by abrupt changes in orientation and a complex bathymetry. The coastline is oriented approximately 10°N on the east side (see Figure 1), which is reoriented to 166°N at the Cape Hatteras point, transitioning to an orientation of 120°N farther west. These two sides around the cape point, with distinctly different coastline orientations, are subsequently referred to as the east and south sides, respectively. The bathymetry in the area is complex, consisting of a shoal (Diamond Shoals) that extends from the cape point to some 20 km offshore toward the SE (see Figure 1d). On the east side and farther away from the shoal, the bathymetric profile (see Transect 1 in Figure 1c) reveals a typical barred beach with an inner and an outer bar. The beach slope varies from 0.040 inshore of the inner bar to 0.004 offshore of the outer bar. Farther south and closer to the shoal (see Transect 2 in Figure 1c), the bathymetry is more complex due to the presence of obliquely aligned transverse ridges. A transect from Cape Hatteras point along the axis of Diamond shoals (see Transect 3 in Figure 1c) reveals a foreshore slope of 0.040 and an irregular bathymetry farther offshore. On the other hand, the south side is characterized by a relatively simple beach profile consisting of a single inner bar (see Transects 4 and 5 in Figure 1c). The foreshore slope is 0.030, and reduces to 0.004 farther offshore.

[7] Wave and current data were collected at 13 locations dispersed throughout the study area (see Figure 1 and Table 1). Three of the sites (O1, O2, and O3) were at relatively deeper water depths of approximately 9–10 m. The remaining of the stations were located in the nearshore with four of them (N1 to N4) located on the east side, two (N11 and N12) on the south side, and the remaining four stations (N5, N6, N8, and N9) over the shoal itself. The instrumentation consisted of acoustic current meters (Nortek Aquadopp and Teledyne RDI ADCP profilers) programmed to resolve both mean and wave-induced flows by measuring three-dimensional flow velocities (bin size 40 cm) and pressure fluctuations with a sampling frequency of 1 Hz. The type of acoustic instrument for each station, their deployment depth, and other details relating to the data collection are listed in Table 1. The Aquadopps collected data continuously while the ADCPs were deployed in a burst data collection mode, recording 1024 data points every hour, centered on the hour. Details of the instrumentation deployment and other auxiliary measurements not presented in this manuscript can be found in *List et al*. [2011].

[8] The continuous records from the Aquadopp instruments were divided in 1024 s segments centered on 0, 15, 30, and 45 min past the hour. This segmentation resulted in a 24 s overlap between adjacent segments. ADCP data were already available in bursts of 1024 s centered on the hour resulting in simultaneous hourly data from all instruments. Instantaneous pressure (p) and horizontal (u, v) velocities from the bin closer to the sea bed were used to calculate power spectral and cross-spectral densities using *Welch*'s [1967] method of spectral estimation using 15 ensembles of 128 data points with 50% overlap. The pressure spectra were converted to sea surface elevation spectra after correcting for pressure attenuation with depth using linear wave theory [*Bishop and Donelan*, 1987]. The sea surface power spectral density and cross spectral density values were then used to calculate the wave height, period, direction, and directional spreading using the moments method [*Herbers et al*., 1999]. Identification of wave energy and directional characteristics for swell and wind waves was carried out by integrating the wave spectra over the frequency bands below and above 0.1 Hz, respectively.

[9] Mean flows were estimated by averaging the instantaneous flows measured within each 1024 s segment. In addition, mean flows from all the bins were linearly extrapolated to the surface and seabed, and then averaged to obtain estimates of depth-averaged mean flows. Finally, these depth-averaged flows were low-pass filtered [*Beardsley et al*., 1985] to remove tidal and other oscillations occurring at periods less than 33 h. Meteorological data for the deployment period and offshore wave data were obtained from the NOAA/NDBC Diamond shoals buoy (ID 41025, Figure 1b).

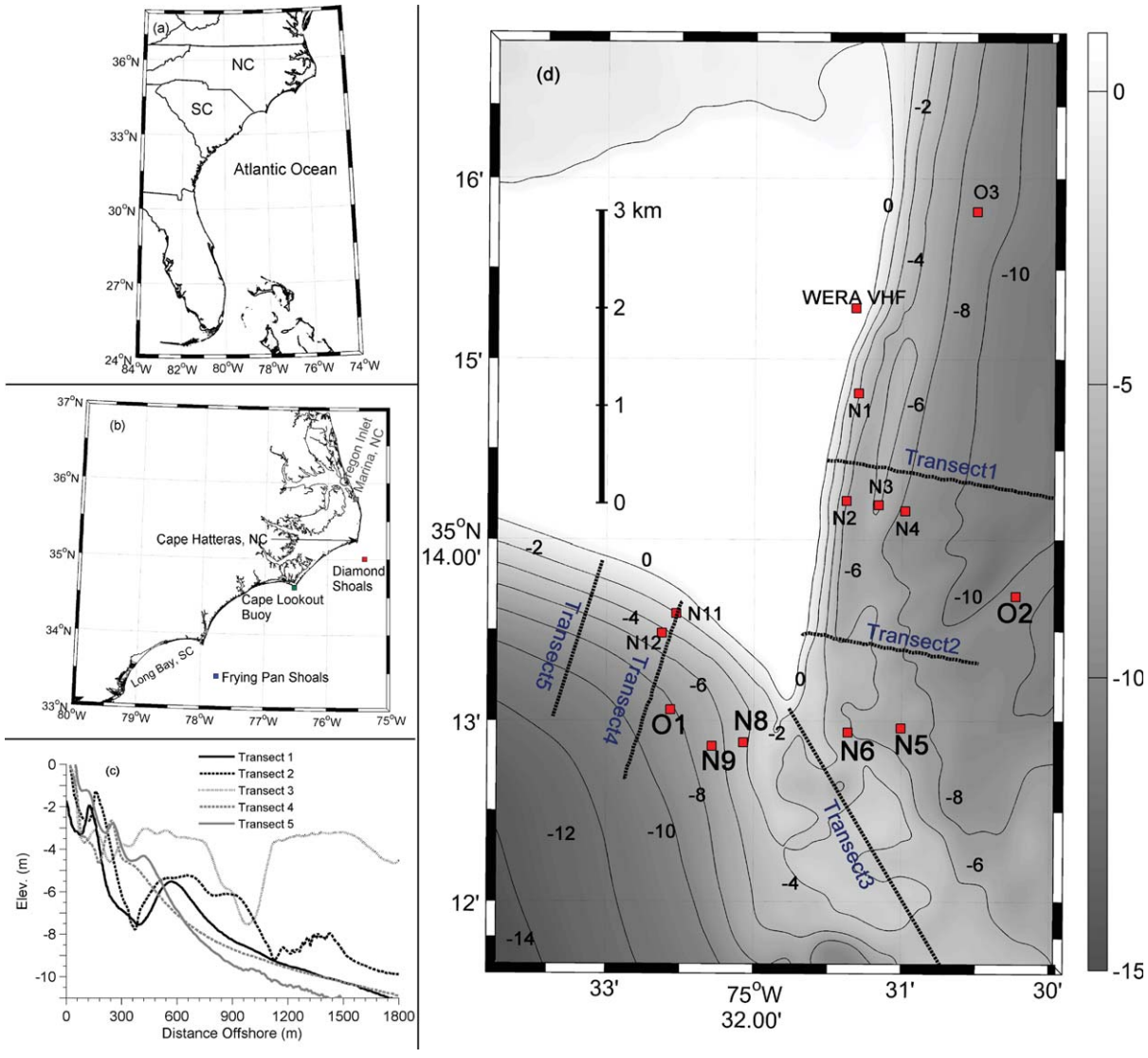

Figure 1. Map showing the study area (Cape Hatteras, NC), the nearshore bathymetry and data collection sites. Bathymetry contours shown are in meters. The prefix "N" and "O" in the station names suggest nearshore (mean water depth less than 8 m) and offshore sites, respectively. The stations used in the analyses are shown with a larger font. Solid black lines are the transects along which the beach profiles are provided in Figure 1c. The location of the NOAA Diamond Shoals buoy is shown in Figure 1b.

3. Results

[10] In this section, the filtered, subtidal flows and wave data are presented together with the atmospheric conditions prevailing during the data collection period. Primarily, data from sites O2, O1, N5, N6, N9, and N8 are presented because of their deployment locations, which are optimal for resolving momentum balance forces in the alongshore direction. Data from other sites (O3, N1, N2, N3, N4, N11, and N12) are discussed briefly in order to provide a general idea of flow field within the study area.

3.1. Offshore Conditions

[11] Time series of the offshore meteorological and wave conditions from NOAA Buoy 41025 during the data collection period are shown in Figure 2. Three high wave energy events are identified that coincide with the passage of two warm and one cold front systems (Figure 2a). The passage of the first warm front system occurred during 5–7 February 2010 (referred to as Event F1), and is characterized by wind speeds in excess of 12 m s^{-1} directed toward the southwest initially and rotating toward the northeast later on (Figure 2a). The maximum offshore wave height recorded was 6 m (Figure 2b) with periods varying from 5 to 10 s (Figure 2d). This event was associated with a drop in atmospheric pressure (Figure 2e) and an increase in air temperature (Figure 2f). This event was followed by a cold front system (10–12 February 2010, Event F2), with winds from the north/northwest initially, changing to east/southeast later on; the maximum wave height recorded was 3 m. After the passage of this second frontal system, increased wave energy concentrated mainly on the swell wave band (Figure 2c) is observed. The two periods (7–9 and 12–13 February 2010) when the ratio of swell to sea wave energy

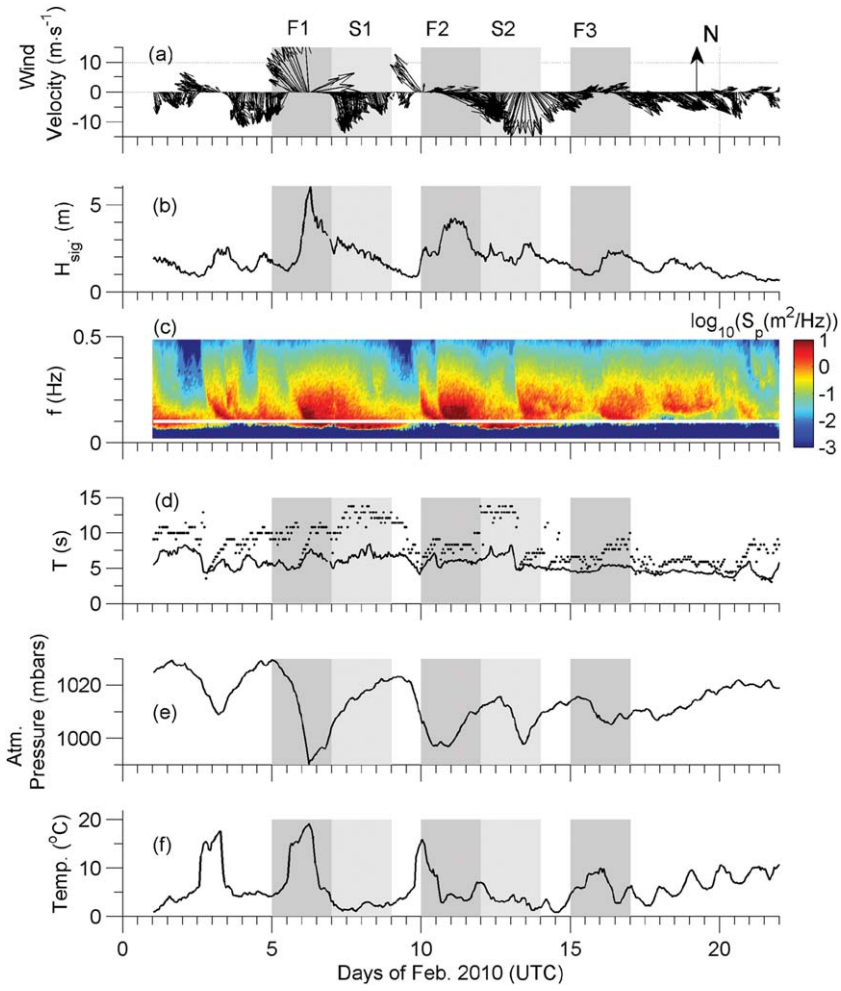

Figure 2. Meteorological and wave data from the Diamond Shoals buoy (NOAA/NDBC Station ID: 41025) for February 2010. Time series of (a) wind velocity vector in oceanographic convention, (b) significant wave height, and (c) surface wave spectrum (m^2/Hz). The 0.1 Hz cutoff used to separate sea and swell frequencies is also shown; (d) peak (black dots) and mean (solid black line) wave period); (e) atmospheric pressure (solid black line); and (f) air (black) temperature. Dark gray shaded areas correspond to passage of synoptic meteorological fronts, and light gray shaded regions are the swell events.

is greater than 1.25 are referred to as swell events and denoted with S1 and S2, respectively. The wave height measured at the offshore buoy during these events (Figure 2b) varied between 2 and 3 m. The third event (15–16 February 2010, Event F3) was due to a warm front similar to event F2 but of reduced intensity.

3.2. Nearshore Conditions

[12] Time series of mean water depth, root mean square wave height (H_{rms}), peak (T_p), and mean (T_m) wave periods, and mean wave direction (measured clockwise from north) estimated from the data collected at sites O2, N5, and N6, located on the east side of the Cape Hatteras point are shown in Figure 3 (left). Water depth variation is primarily due to tides (Figure $3a_1$), while the wave height (Figure $3b_1$) varied between 0.5 m and 3 m for the entire data collection period with the peak wave period fluctuating between 5 s and15 s (Figure $3c_1$). Swell waves ($T_p > 10$s) approached the shoreline from the northeast (see Figure $3d_1$) while gravity wind waves ($T_p < 10$ s) tended to approach from the east-southeast. During periods of low wave activity (see 16–22 February 2010), both wave height (Figure $3b_1$) and direction (Figure $3d_1$) show a tidal modulation, revealing the influence of wave refraction and depth-limited leakage of wave energy over the shoal.

[13] The most energetic wave events in the records are associated with the passage of the first warm front (event F1) and the swell event S1. During event F1, negligible cross-shore variability in wave height is observed between stations O2, N5, and N6, while the wave height reduces substantially as it approaches the shore during event S1 (Figure $3b_1$). The dissipation of wave energy per unit distance from site O2 to N5 is three orders of magnitude higher than typical dissipation rate of swell waves due to bottom friction [e.g., *Herbers et al.*, 2000], suggesting dissipation of wave energy between these sites primarily occurs due to depth limited wave breaking. The wave forcing during other frontal passages (event F2 and F3) were similar to event F1, but less energetic when compared to event F1.

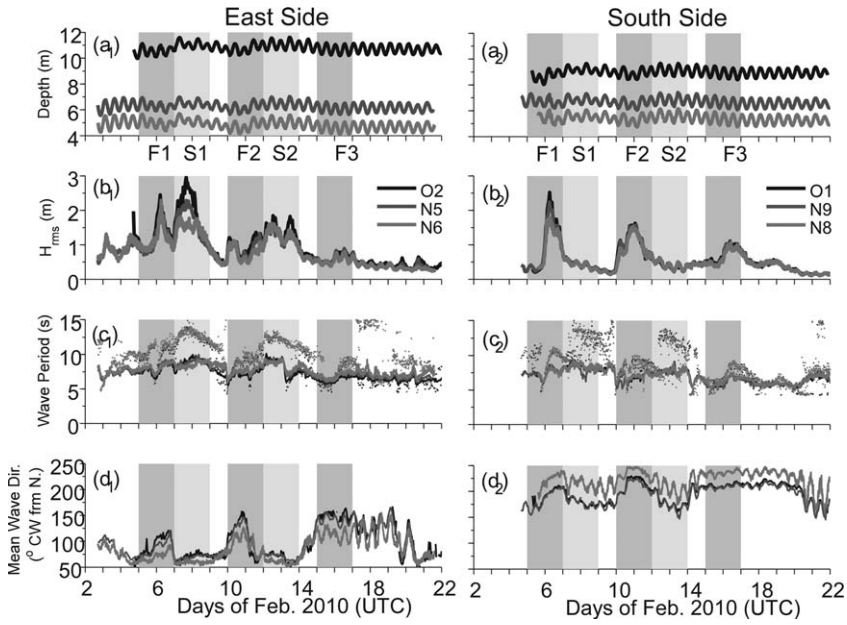

Figure 3. Time series of (a) water depth, (b) root mean square wave height, (c) peak (dots) and mean (solid) wave period, and (d) mean wave direction (°N) for the east (left, subscript 1) and south sides (right, subscript 2), respectively. The shaded areas indicate periods of frontal passage (dark gray shade) and swell events (light gray shade) as in Figure 2.

[14] In contrast to the conditions recorded on the east side, on the south side (Figure 3, right column) smaller wave heights were observed (0.5–2.5m) with peak wave periods ranging from 5 to 15 s. The general wave direction (Figure $3d_2$) was consistently from the southwest for all events with the highest wave conditions recorded during event F1 (5–7 February 2010). A similar but weaker response is seen during the passage of the other two fronts (10–12 and 15–16 February). Interestingly, in this (south) side, the height of the swell waves during events S1 and S2 was small (Figure $3b_2$), while mean swell direction varied from south to southwest. The tidal modulation of swell direction on the south side suggests refraction of swell waves around the shoal. This combined with dissipation due to bottom friction and depth limited wave breaking over the shoal, leads to a significantly reduced swell height when compared with that recorded on the east side for the same events.

3.3. Subtidal Flows

[15] The low pass filtered wind stress exhibits large variability (Figure 4) around its mean value, with the principal axis of the variance ellipse being almost perpendicular (120°) to the coastline on the east side and almost parallel to the coastline orientation further west of the cape point. The strongest flows were measured at site N6 with a southward mean direction. The principal axes of the subtidal flow variance ellipses at sites O3, N1, N2, N3, N4, and O2 are parallel to the local coastline orientation (Figure 4); at sites N5 and N6, the ellipse is rotated and aligned with the local bathymetric contours that define the orientation of the shoal itself (see Figure 4). Also, the eccentricity of the ellipses in these sites decreases, indicating the existence of some cross-shoal flows. Furthermore, it is worth noting that the mean flows at N1, N5, and N6 do not align with the major axis of the subtidal ellipse possibly due to bathymetric rectification.

[16] On the south side, the variance ellipses are aligned to the local coastline orientation away from the shoal (i.e., sites N11 and N12), while at sites O1, N8, and N9, the orientation of the principal axis becomes parallel to the bathymetric contours. The mean flows at all sites on the south side are obliquely oriented to the ellipse semimajor axis with the exception of site N11.

[17] In order to examine the balance of wind and hydrodynamic forcing, the depth-averaged subtidal flow and wind vector components are rotated into two local coordinate systems corresponding to the respective local coastline orientations (10° and 166°N) for the east and south sides, respectively (see Figure 4). In each one of these new coordinate systems, positive cross-shore velocity values indicate offshore directed flows while positive alongshore velocities indicate northeastward flow at the east side and southeastward flow at the south side. Correlation coefficients (r) between the alongshore and cross-shore components of wind stress and measured flow (subsampled with a decorrelation time scale of 33 h, see section 4.2) for each site are presented in Table 2.

[18] Local cross-shore wind stress shows a negative correlation with alongshore flows on both sides of the cape with those on the south side being larger (-0.67 to -0.77) than those on the east side (-0.29 to -0.51, not significant at 95% CI). On the other hand, local alongshore wind stress is highly (0.83 to 0.90) and moderately (0.54 to 0.63) correlated with alongshore flows on the east and south sides, respectively. Correlation of the wind components with the cross-shore flows is generally variable with strong and statistically significant correlations (see Table 2) found only at site N8.

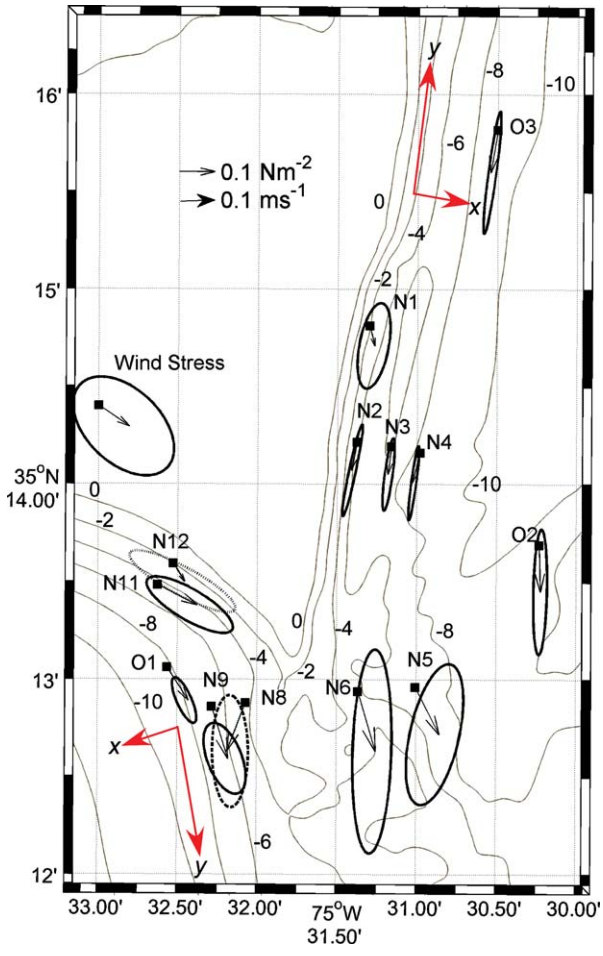

Figure 4. Synoptic description of wind forcing and depth-averaged subtidal currents described by their mean (black arrows) and vector variance ellipses for the full period of data collection for each site (see Table 1). The local coordinate (x, y) systems used at each side are also shown.

[19] In the east side, at sites O2, N5, and N6 the alongshore flow responds to the alongshore wind stress with a small time lag (~1 h) during all events (Figures 5a$_1$ and 5b$_1$). The highest alongshore and cross-shore current speed were measured during events F1 and S1 (Figures 5b$_1$ and 5c$_1$), while the flow response was weaker for all other events. In the south side, although the highest alongshore wind stress occurs during event F1, the subtidal response of the alongshore flow (at sites N9 and O1) is relatively weak (< 0.2 m s^{-1}) and with a direction opposite of that of the wind (Figure 5b$_2$). Alongshore current velocities at site N8 are of the same magnitude as those at site N9 but they are directed toward the northeast. For events F2 and F3, the data from sites O1, N9, and N8, show a direct response of the alongshore flows to the wind stress, while cross-shore flows are usually negligible except at site N8 during event F2 (Figure 5b$_2$).

[20] Overall, circulation on the east side of Cape Hatteras point appears to be driven primarily by wind stress, while on the south side wind stress alone does not seem to be adequate to explain the observed circulation. These flows are further examined through a depth-averaged, alongshore momentum balance analysis which is presented next.

4. Momentum Balance Analysis

[21] The goal of this section is to identify the drivers of observed circulation patterns on both east and south side of Cape Hatteras using a depth-averaged form of the momentum balance equations presented in *Kumar et al*. [2012]. In comparison to *Lentz et al*. [1999], these equations contain two more terms: (a) Stokes-Coriolis force (effect of Earth's rotation on surface gravity waves) and (b) the horizontal component of vortex force (interaction between Stokes drift and mean flow vorticity). In its full flux form, the depth-averaged alongshelf momentum balance equation can be written as:

$$\underbrace{\frac{\partial \overline{v}}{\partial t}}_{\text{LA}} + \underbrace{f\overline{u}}_{\text{CA}} + \underbrace{f\,\overline{u^{St}}}_{\text{SC}} + \underbrace{\frac{1}{h}\frac{\partial}{\partial x}\left(\int_{-h}^{0}(uv)\,dz\right) + \frac{1}{h}\frac{\partial}{\partial y}\left(\int_{-h}^{0}(vv)\,dz\right)}_{\text{NA}} + \underbrace{\frac{\overline{u^{St}}}{h}\left\{\frac{\partial}{\partial x}\left(\int_{-h}^{0} v\,dz\right) - \frac{\partial}{\partial y}\left(\int_{-h}^{0} u\,dz\right)\right\}}_{\text{VF}} + \underbrace{\frac{\tau_{by}}{\rho_0 h}}_{\text{BS}}$$
$$= \underbrace{\frac{-1}{\rho_0}\frac{\partial p}{\partial y}}_{\text{APG}} + \underbrace{\frac{\tau_{sy}}{\rho_0 h}}_{\text{SS}} - \underbrace{\frac{1}{\rho_0 \cdot h}\cdot\frac{\varepsilon_b \cdot k_y}{\sigma}}_{\text{BA}} \qquad (1)$$

[22] where u and v are the cross-shore and alongshore subtidal velocity components with the overbar denoting depth averaging; z is the elevation above mean sea level; h is water depth; f is the Coriolis parameter ($=8.43\times10^{-5}$ s^{-1}); and ρ_o is the reference density ($=1024$ kg m^{-3}).

[23] In this study, the various terms of equation (1) are estimated using data from sites O2, N5, N6, O1, N9, and N8. Estimation of the nonlinear (NA) and VF terms require the calculation of gradients in the cross-shore (x) and alongshore (y) directions. Although cross-shore gradients were estimated (see section 4.1), the instrument layout did not allow us to obtain reliable alongshore gradients for the majority of the sites. However, a comparison of depth-averaged alongshore velocities between site pairs (O2, O3) and (N3, N5) did not reveal any substantial alongshore gradient and therefore we have assumed that these terms are negligible. In addition, due to low resolution of the pressure sensors installed on the acoustic current profilers no

Table 2. Correlation Coefficient (r) Between Wind Stress and Local Alongshelf (v) and Cross-Shore (u) Velocity Components[a]

	Site					
Local Wind Stress Component	East Side			South Side		
	O2	N5	N6	O1	N9	N8
τ_x	*u*, *v* *0.2*, −0.5	*u*, *v* *−0.4*, *−0.4*	*u*, *v* *−0.2*, *−0.3*	*u*, *v* *0.1*, −0.8	*u*, *v* *−0.2*, −0.8	*u*, *v* −0.8, −0.8
τ_y	*−0.5*, 0.9	*0.4*, 0.9	*−0.2*, 0.8	*0.1*, 0.6	*0.4*, 0.6	0.8, 0.5

[a] *r* values in italics are not significant at the 95% confidence level.

accurate pressure gradient terms could be estimated, thus we elected to omit these terms as well. These assumptions allow us to simplify equation (1) to (see *Lentz et al*., 1999; *Kumar et al*., 2012]:

$$\frac{\partial \overline{v}}{\partial t} + f\overline{u} + f\overline{u^{St}} + \frac{1}{h}\frac{\partial}{\partial x}\left(\int_{-h}^{0}(uv)dz\right) + \frac{\overline{u^{St}}}{h}\left\{\frac{\partial}{\partial x}\left(\int_{-h}^{0} v dz\right)\right\} + \frac{\tau_{by}}{\rho_0 h} = \frac{\tau_{sy}}{\rho_0 h} - \frac{1}{\rho_0 \cdot h}\cdot\frac{\varepsilon_b \cdot k_y}{\sigma} \tag{2}$$

4.1. Calculation of Alongshore Momentum Balance Terms

[24] The local acceleration term $\partial v/\partial t$ is calculated using a forward differencing scheme although usage of a central differencing method did not provide any different results from what is shown here. The Coriolis acceleration is obtained as a product of Coriolis parameter and subtidal, depth-averaged cross-shore currents.

[25] Wind stress is estimated using the wind data from NOAA-NDBC Diamond shoals buoy (see location in Figure 1b) utilizing the neutral drag law of *Large and Pond* [1981] after correcting for the elevation of the wind sensor

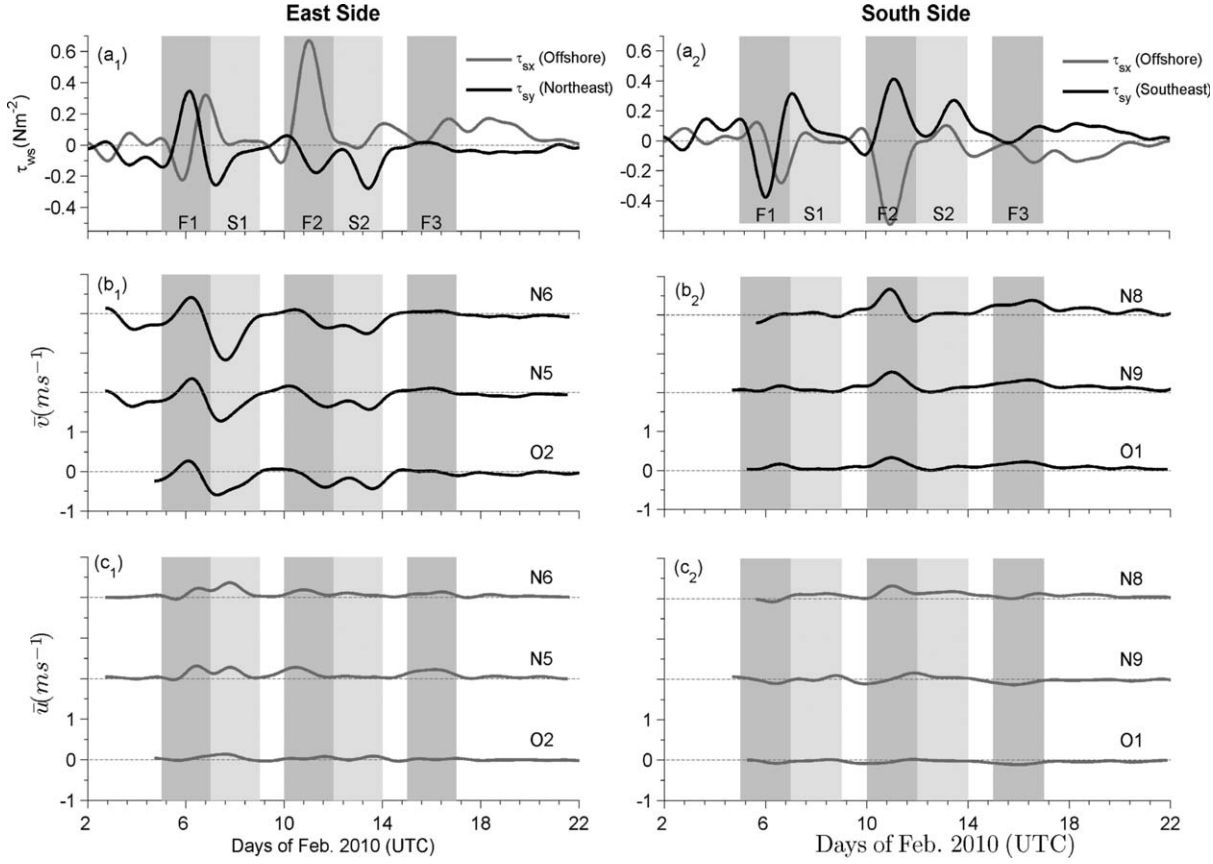

Figure 5. Time series of local (a) subtidal alongshore (solid black) and cross-shore (solid gray) wind stress, (b) alongshore, and (c) cross-shore currents on the east (left, subscript 1) and the south side (right, subscript 2). The vertical scale in Figures 5b and 5c is shifted vertically for each station for clarity. Dark and light gray shaded regions correspond to the periods of frontal passage and swell events, respectively. The coordinate systems for the east and south sides are shown in Figure 4.

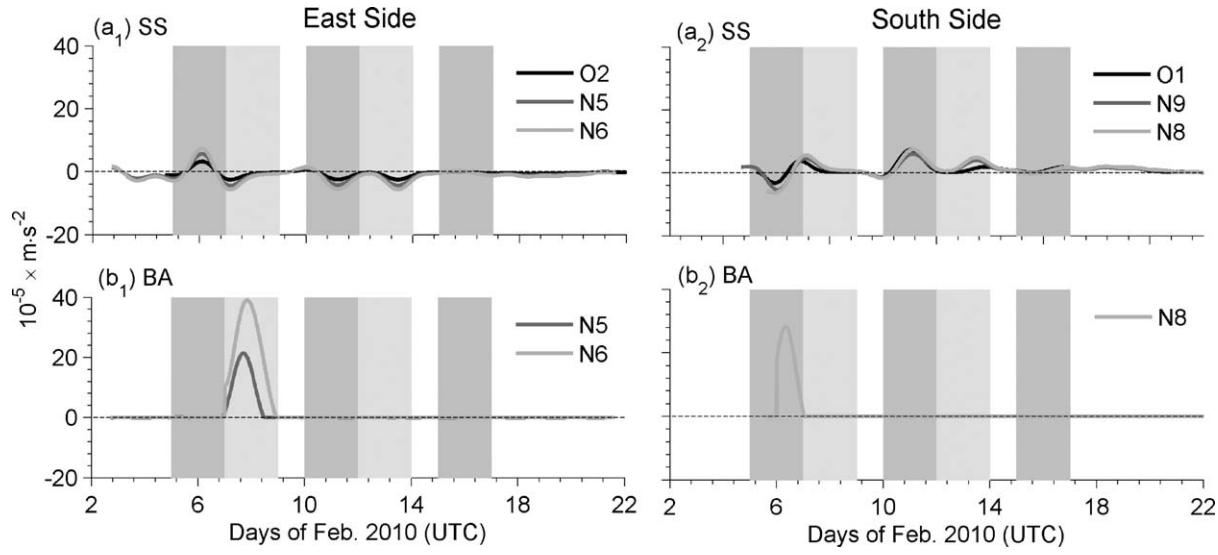

Figure 6. Time series of low-pass filtered (a) surface stress, (b) breaking-induced acceleration for the east (left, subscript 1) and south (right, subscript 2) sides. No depth-limited wave breaking was observed a site O2, O1, and N9 during the deployment period.

above the sea surface and accounting for the influence of waves [*Large et al*., 1995]. It is assumed that the wind velocity remains uniform over the entire study area as the vector correlation between winds measured at Diamond Shoals and Oregon Inlet some 90 km away (see Figure 1b) was found to be 1.56 [*Crosby et al*., 1993].

[26] Bottom stress is estimated using the method of *Styles and Glenn* [2000] that accounts for enhanced roughness due to the presence of waves, a process which becomes important in shallower inner shelf waters as is the case in here. The Stokes-Coriolis force term was calculated using a depth-averaged Stokes velocity derived from the directional wave properties estimated from the wave measurements at each site using:

$$\overline{\boldsymbol{u}}_{St} = \frac{gH_{sig}^2}{16ch}\hat{\boldsymbol{k}} \tag{3}$$

where H_{sig} is the significant wave height, g is the acceleration due to gravity, c is the phase speed of wave, h is the water depth, and $\hat{\boldsymbol{k}}$ is the unit wave vector.

[27] When no data with high spatial resolution are available, the NA and VF terms can be estimated assuming a no flux condition at the coastline as in *Fewings* [2007] and *Kirincich and Barth* [2009]. This method assumes that the alongshore and cross-shore velocities decrease monotonically from the most inshore measurement site to the no flux point at the coastline and as such is highly sensitive to location of the inshore station in relation to the coastlines and the shape of the bathymetric profile. Shoaling waves and surf zone dynamics suggest the existence of a maximum in longshore currents (and associated flux) inside the surf zone which is missed if the inshore station is farther offshore. In order to identify that maximum velocity and obtain a better approximation of the NA and VF terms, a linearized alongshore momentum balance equation is used to calculate cross-shore distribution of depth-averaged alongshore velocity (v, see section 5.3). This basic equation does not consider the NA and VF terms while bottom stress is approximated as a linear drag. This method assumes that wave breaking induced acceleration (obtained from a third generation wave propagation model simulating waves nearshore, *Booij et al*. [1999], section 5.3) and wind stress are the only forcing terms.

[28] The VF term is calculated from the simplified model as the product of the depth-averaged, cross-shore Stokes drift obtained from the wave parameters (equation (3)) and cross-shore gradient of depth-averaged alongshore velocity ($\overline{u^{St}}\cdot\partial\overline{v}/\partial x$), while NA is approximated at each site as the product of measured depth-integrated cross-shore velocity and the estimated cross-shore gradient of depth-averaged alongshore velocity ($\overline{u}\cdot\partial\overline{v}/\partial x$). At this point, we should mention that these estimates have similar magnitude as those obtained directly from field observations assuming no flux conditions at the coastline (not shown here).

[29] Finally, following *Lentz et al*. [1999], the breaking-induced acceleration term shown in equation (2) is estimated from the directional wave properties measured at each site using the wave dissipation model of *Church and Thornton* [1993]:

$$\varepsilon_b = \frac{3\sqrt{\pi}}{16}\cdot\rho_0\cdot g\cdot\frac{B_b^3\cdot f_p}{h}\cdot H_{rms}^3\cdot\left[1+tanh\left\{8\cdot\left(\frac{H_{rms}}{\gamma_b\cdot h}-1\right)\right\}\right]^{-5/2}\cdot\left[1-\left\{1+\left(\frac{H_{rms}}{\gamma_b\cdot h}\right)^2\right\}\right] \tag{4}$$

which is subsequently used to estimate the breaking-induced acceleration:

$$\mathrm{BA} = \frac{1}{\rho_0\cdot h}\cdot\frac{\varepsilon_b\cdot k_y}{\sigma} \tag{5}$$

where H_{rms} is the root mean square wave height; f_p is the peak wave frequency; σ is the angular frequency ($2\pi f_p$); k_y is the alongshore component of wavevector ($\boldsymbol{k}$); g is the

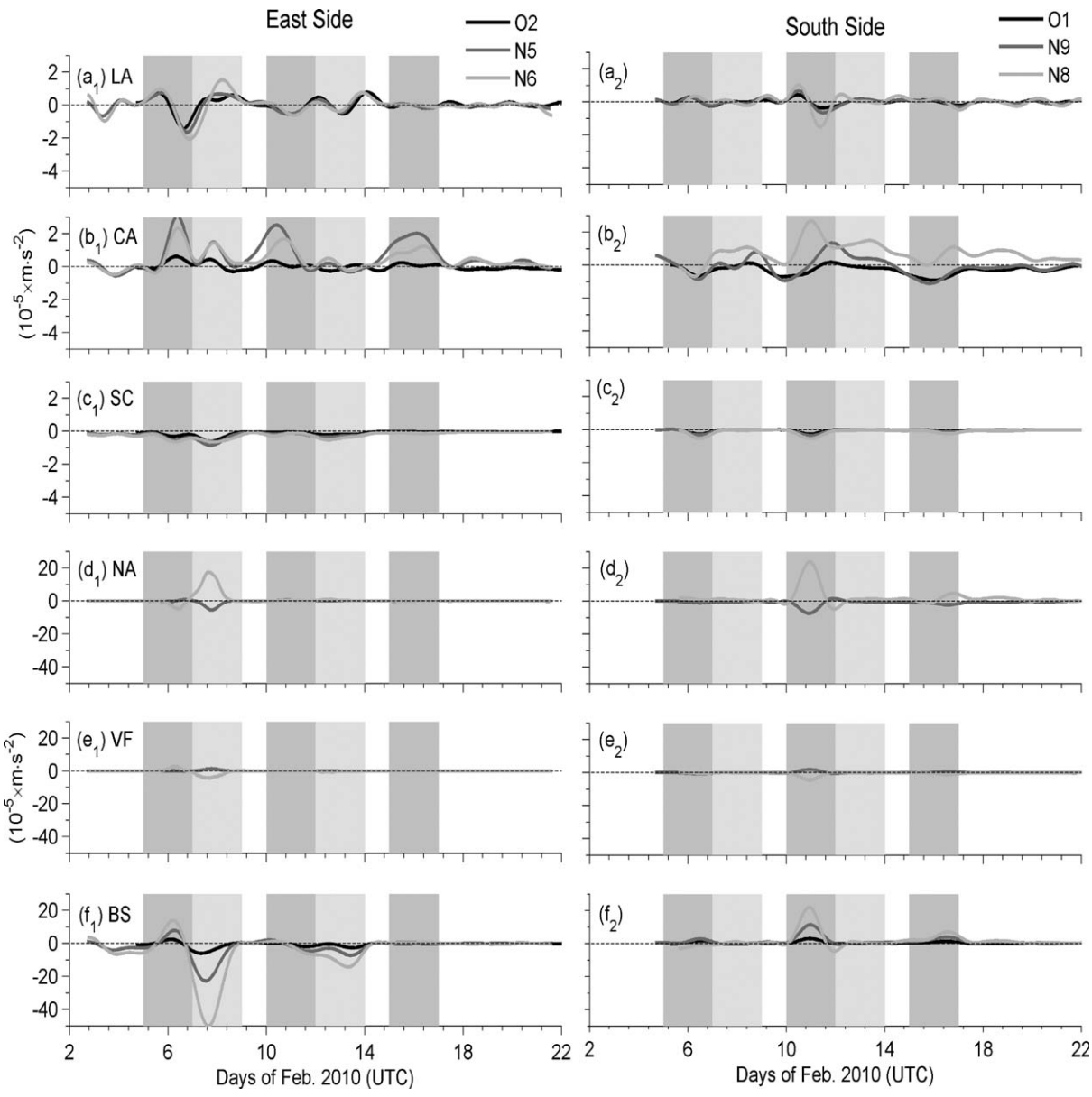

Figure 7. Time series of low-pass filtered response terms in depth-averaged alongshore momentum balance (equation (2)) for the east (left, subscript 1) and south (right, subscript 2) sides and for different sites (see key). (a) Local Acceleration, (b) Coriolis acceleration, (c) Stokes-Coriolis force, (d) nonlinear advective acceleration, (e) vortex force, and (f) bottom stress. Please note that the vertical scales in Figures 7d–7f, are 10 times the vertical scale in Figures 7a–7c.

acceleration due to gravity. B_b (= 0.72) and γ_b (=0.24 to 0.40) are empirical parameters [e.g., *Chen et al*., 1997] that depend on beach profile type and wave conditions. Using this method, wave breaking conditions were identified during the periods 7–9 and 5–7 February 2012 for the east (sites N5 and N6) and south (site N8) sides, respectively (Figures $6b_1$ and $6b_2$), with γ_b values ∼0.30. When wave breaking is not evident, the breaking-induced acceleration term is set to zero.

4.2. Depth-Averaged, Simplified Alongshore Momentum Balance

[30] The time-series of the momentum balance terms shown in equation (2) are displayed in Figures 6 and 7 for both east and south sides. Considering that the mean values of most of these terms are close to zero, their standard deviation (see Table 3) provides an indication of the term's relative importance. Overall, bottom stress (BS), surface stress (SS), breaking-induced acceleration (BA), nonlinear advective acceleration (NA), and vortex force (VF) have high standard deviation values, while the contribution of local (LA), Coriolis (CA), and Stokes-Coriolis (SC) acceleration is smaller, except at site N5 where VF is of the same order as LA, CA, and SC.

[31] The temporal and spatial variability of the alongshore momentum balance terms provide some additional insights on the response of the shelf during this experiment. Both the LA (Figures $7a_1$ and $7a_2$) and CA (Figures $7b_1$

Table 3. Standard Deviation of Local Alongshore Depth-Averaged Momentum Balance Terms[a]

	East			South		
Term	O2	N5	N6	O1	N9	N8
Local acc. (LA)	3.3	4.2	5.8	1.5	2.1	3.6
Coriolis acc. (CA)	2.0	8.4	5.8	2.7	5.3	6.0
Stokes-Coriolis acc. (SC)	1.2	1.9	1.8	0.7	0.9	1.4
Nonlinear acc. (NA)	–	10.7	48.5	–	13.7	44.9
Vortex force (VF)	–	1	24.9	–	3.9	8.7
Bottom stress (BS)	14.0	50.6	108.8	6.7	23.1	43.9
Surface stress (SS)	8.0	17.4	22.4	17.2	18.8	23.8
Breaking acc. (BA)	0	39.0	157. 8	0	0	49.6

[a]No values are shown for terms/site combinations which could not be calculated. All units in 10^{-6} m s^{-2}.

and $7b_2$) terms respond to wind and wave forcing. The Stokes-Coriolis term (Figures $7c_1$ and $7c_2$) becomes important during both front and swell events due to increased wave activity. In deeper waters (e.g., site O2), its magnitude is similar to Coriolis acceleration during swell events. The NA and VF terms, both become important only during the first front (event F1) and swell event S1 (see Figures $7d_1$, $7e_1$, $7d_2$, and $7e_2$). The magnitude of these latter terms is higher at sites N6 and N8 than at sites N5 and N9 while the NA term is usually slightly greater than VF.

[32] A rearrangement of the terms in equation (2) into forcing and response ones allows us to examine the two groups separately. Although there is no strict definition of "forcing" and "response", in here we define as forcing the terms that can drive flow (i.e., terms that do not depend on velocity, i.e., wind and waves). The remainder terms that depend on velocity (alongshore or cross-shore) are considered to represent the response of the system to the forcing. It should be noted that since part of NA can be balanced by VF (see Figures $7d_1$, $7d_2$, $7e_1$, and $7e_2$; *Kumar et al.* [2012]), in this analysis, the NA and VF terms are added together and their sum is treated as a single term.

[33] Initially, the correlation between the SS (representing forcing) and BS (representing response) terms is estimated. Subsequently, the breaking-induced acceleration (BA) term is added to SS and then compared against BS. If the correlation between forcing and response improves, then BA is retained as a forcing term, alternatively is rejected. After identifying the terms constituting the forcing, the same method is followed for the response with each term being added to BS and retained only if it contributes to increasing the correlation between the net forcing and response terms. The correlation coefficient (r) estimates in this analysis have been corrected for the decorrelation time of our data. Using *Garrett and Toulany* [1981, their equation (8.1)], we estimated a wind forcing decorrelation time scale ~20 h. However, being conservative and considering that all data presented in this study have been low-pass filtered, we elected to adopt the filter's cut-off period (33 h) as the appropriate decorrelation time scale. This assumption makes the number of independent data points to vary from 12 (for the shorter deployment site N8) to 33 for the longer deployment site (i.e., site O2). The critical correlation coefficient to determine if the correlation obtained is significant ($\neq 0$) at 95% confidence interval are 0.56 and 0.33 for a sample size of 12 and 33, respectively.

Table 4. Correlation Coefficient (r) Between Bottom Stress (BS) and Forcing Terms of Depth-Averaged Momentum Balance[a]

			Forcing	
	Site	BS	SS	SS+BA
East	O2		0.74	–
	N5		0.50	0.83
	N6		*0.33*	0.88
South	O1	↓	0.91	–
	N9		*0.11*	–
	N8		0.63	0.68

[a]r values in italics are not significant at the 95% confidence level. SS, surface stress; BA, breaking-induced acceleration.

[34] The analysis of estimating forcing and response terms is conducted for both sides and the results are listed in Tables 4 and 5 for the forcing and response, respectively, while a description for each side is presented separately in the following two subsections.

4.2.1. East Side

[35] At site O2 (depth ~10 m), the major balance is between surface stress (SS) as forcing and bottom stress (BS), Stokes-Coriolis (SC) and Coriolis Acceleration (CA) as response which correspond to a correlation with $r = 0.79$. A regression between the forcing and the sum of the response terms (BS+SC+CA) reveals a slope close to 1 (see Table 6), with BS dominating the response (Figure $8a_1$).

[36] In shallower water depths (depth ~6 m, site N5), the bottom stress is moderately correlated to surface stress ($r = 0.50$, see Table 4) but when breaking-induced acceleration is added to the surface stress, the correlation improves ($r = 0.83$, see Tables 4 and 5). Adding the smaller in magnitude VF, NA, and SC terms at site N5 in the response group (see Figs. $7c_1$, $7d_1$, and $7e_1$) slightly improves the correlation providing a correlation coefficient between force and response of 0.86 and a slope of 1.0 (Table 6) suggesting that BS+VF+NA+SC $\approx$ BA+SS (Figure $8b_1$). The same balance is identified for even shallower waters (i.e., 5 m, at site N6, see Tables 5 and 6 and Figure $8c_1$).

[37] Overall, on the east side of the cape, the shallower parts of the inner shelf respond to forcing provided by both wind (SS) and waves (BA). These two forcing parameters are usually interrelated during periods of storm activity like the frontal events identified in here, but in the case of swell dominance this is not the case. The response is exhibited mainly through bottom stress (BS), nonlinear advective acceleration (NA), and vortex force (VF) (also see section 5.3). In deeper waters (~10 m), the surface and bottom stress almost balance each other.

4.2.2. South Side

[38] Unlike the east side, the alongshore momentum balance on the south side is more complex. At site O1 (water depth ~ 9 m) surface and bottom stresses (Figures $6a_2$ and $7f_2$) are strongly correlated ($r = 0.90$, Table 4). Adding LA to BS as a response term (Figure $7a_2$) reduces this correlation, while adding CA and SC (Figures $7b_2$ and $7c_2$) marginally improves r to 0.91 (Table 5). The slope of the regression line of forcing (wind stress only) and response defined as the sum of bottom stress and Coriolis

Table 5. Correlation coefficient (r) between forcing and response terms of depth-averaged momentum balance[a]

			Response Terms					
Site		Forcing Terms	BS	BS+SC	BS+SC+CA	BS+SC+CA+LA	BS+SC+CA+LA+ [NA+VF]	BS+SC+ [NA +VF]
East	O2	SS	0.74	0.76	**0.79**	0.78	–	–
	N5	SS+BA	0.83	0.84	0.76	0.75	0.75	**0.86**
	N6	SS+BA	0.88	0.89	0.87	0.85	0.84	**0.92**
South	O1	SS	0.90	0.89	**0.91**	0.90	–	–
	N9	SS	*0.11*	*0.09*	***0.33***	*0.25*	*0.21*	*0.03*
	N8	SS+BA	0.68	0.68	**0.71**	0.70	0.67	0.65

[a]r values in italics are not significant at the 95% confidence level. Bold typeface values represent the maximum correlation coefficient value for given combination of forcing and response terms. BA, breaking-induced acceleration; NA, nonlinear advective acceleration; VF, vortex Force; SS, surface Stress; BS, bottom Stress; LA, local acceleration; and SC, Stoke-Coriolis term.

Table 6. Slope (m) and Intercept (c) for the Relation $[R = m \cdot F + c]$[a]

Site Name	m	c ($\times 10^{-5}$ m s^{-2})
O2	1.1 ± 0.3	-0.01 ± 0.3
N5	1.0 ± 0.4	-0.3 ± 1.1
N6	1.1 ± 0.1	-0.4 ± 1.2
O1	0.5 ± 0.1	-0.4 ± 0.2
N9	0.2 ± 0.4	1.0 ± 1.1
N8	0.5 ± 0.4	4.4 ± 2.7

[a]F is the forcing term determined from Table 4 to have maximum correlation to the response term (R). 95% confidence interval for m and c are shown. On using the algorithm of *Krystek and Anton* [2007] instead of using a standard linear regression technique, and assuming 50% uncertainty in both forcing and response terms, only slightly modifies the regression coefficients and slopes shown here.

acceleration is only 0.5 (Table 6), indicating that additional terms are needed to close the balance.

[39] At shallower water depths (i.e., 6.5 m, site N9), both VF and NA (Figures 7d$_2$ and 7e$_2$) have the same magnitude as BS but do not correlate to surface stress (SS). The highest correlation (r=0.33, not significant at 95% CI, see Table 5) and regression slope ($m = 0.20$, Table 6) are obtained only when we include CA (Figure 7b$_2$), BS (Figure 7f$_2$), and SC (Figure 7c$_2$) as response to the surface stress (SS) forcing (Figure 6a$_2$). Similar results are obtained for site N8 where response (BS) and forcing (SS+BA) correlate with a coefficient of 0.68 while the regression slope between them is only 0.5.

[40] Unlike the north side, the momentum balance is not closed on the south side as clearly demonstrated by the low regression slopes and correlation coefficients obtained. Furthermore, it is worth noting that at times forcing acts in a direction opposite to what it should be expected from the response (Figures 8a$_2$–8c$_2$).

5. Discussion

[41] The discussion is divided into two sections that attempt to: (a) explain the inability to close the momentum balance on the south side of Cape Hatteras and investigate the relation of this with coastline orientation; and (b) identify the importance of the vortex force term in relation to wave forcing and wind stress.

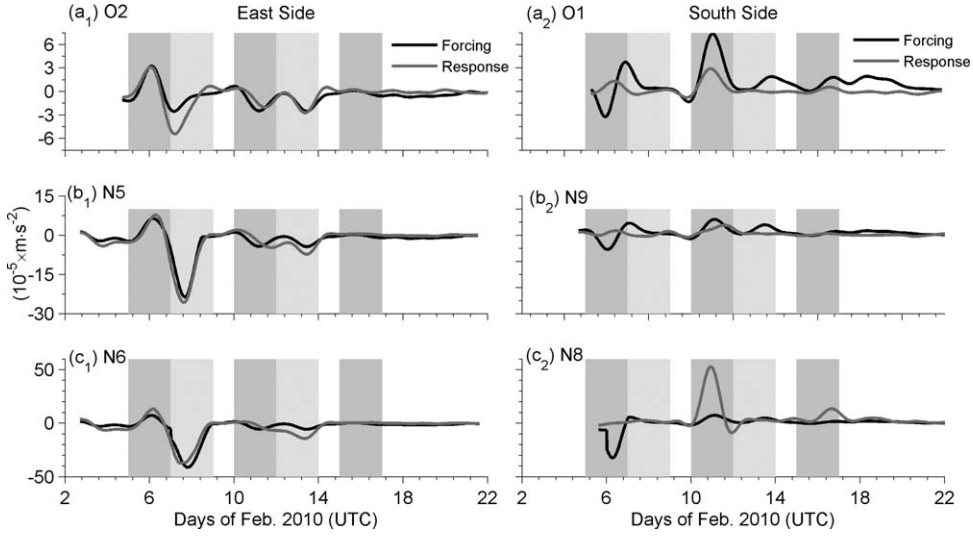

Figure 8. Time series of response (gray) and forcing (black) terms at north (left, subscript 1) and west (right, subscript 2). The relevant forcing and response terms at each site are listed in Tables 4 and 5. Note the different vertical scales used.

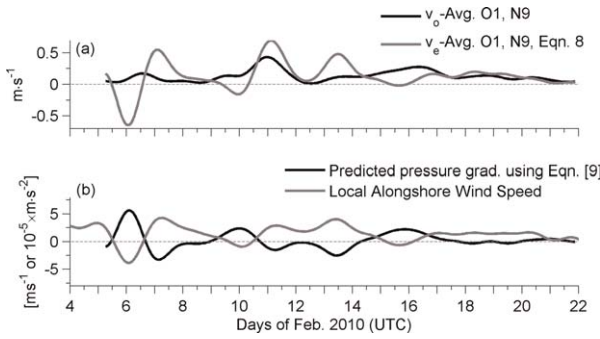

Figure 9. Time series of (a) average (between Site O1 and N9) observed (black) and predicted (gray) alongshore velocity (ms^{-1}); (b) predicted (black) pressure gradient terms and local alongshore wind speed from NOAA-NDBC Diamond shoals buoy (for definition of local coordinate system see Figure 4).

5.1. The Effect of Coastline Orientation

[42] As shown in section 4.2, we were not able to close the alongshore momentum balance on the south side of Cape Hatteras, suggesting the existence of additional forcing that has not been captured by our analysis. One possibility is pressure gradient that was not considered in the analysis. Although this term was not found to be important on the east side, we hypothesize that pressure gradient can play a role on the south side. This hypothesis is explored using a linearized form of the momentum balance equation that can be used to estimate the magnitude of a pressure gradient (PG) term that could close the balance. The alongshore momentum balance equation (equation (2)) is modified so that the PG term is now included and linearized by expressing the bottom stress through a linear bottom drag parameterization [e.g., *Lentz and Winant*, 1986] so that:

$$\frac{\partial \overline{v}}{\partial t} + f\overline{u} + f\overline{u^{St}} + \frac{1}{h}\frac{\partial}{\partial x}\left(\int_{-h}^{0}(uv)dz\right) + \frac{\overline{u^{St}}}{h}\left\{\frac{\partial}{\partial x}\left(\int_{-h}^{0} v dz\right)\right\} + \frac{r\overline{v}}{h} = -g\frac{\partial \eta}{\partial y} + \frac{\tau_{sy}}{\rho_0 h} - \frac{1}{\rho_0 \cdot h}\cdot\frac{\varepsilon_b \cdot k_y}{\sigma} \tag{6}$$

where r is the linear bottom drag coefficient for depth-averaged flows, h is the mean water depth, η is the sea surface elevation and g is the acceleration due to gravity. In section 4.2.2, we showed that both LA and CA are an order of magnitude smaller than the dominant terms (see Figures $7a_2$ and $7b_2$), while NA and VF do not correlate with the observed forcing terms on the south side. On the basis of these findings, we can further simplify equation (6) by ignoring these terms and solve for mean velocity:

$$\overline{v}_o = T_f\left[-g\frac{\partial \eta}{\partial y} + \frac{\tau_{sy}}{\rho_0 h} - \frac{1}{\rho_0 \cdot h}\cdot\frac{\varepsilon_b \cdot k_y}{\sigma} - f\overline{u^{St}}\right] \tag{7}$$

where T_f, a representation of a frictional time scale, is defined as h/r and $\overline{v}_o$ is the observed flow. Equation (7) will be valid for our velocity measurements if all the forcing terms (i.e., BA, SS, and pressure gradient term) are responsible for the observed flows. Ignoring the PG term and considering a balance between dominant forcing and response terms as exhibited through the correlation analysis (section 4.2.2), we can estimate an equivalent velocity ($\overline{v}_e$) such that:

$$\overline{v}_e = T_f\left[\frac{\tau_{sy}}{\rho_0 h} - \frac{1}{\rho_0 \cdot h}\cdot\frac{\varepsilon_b \cdot k_y}{\sigma} - f\overline{u^{St}}\right] \tag{8}$$

where $\overline{v}_e$ represents the magnitude of the flow that should had developed using the measured BA and SS forcing terms alone assuming that pressure gradient was not important. Combining equations (7) and (8), the PG term required to produce the observed flow ($\overline{v}_o$) can be estimated by:

$$-g\left(\frac{\partial \eta}{\partial y}\right) = \frac{\overline{v}_o - \overline{v}_e}{T_f} \tag{9}$$

[43] Using equations (7) to (9), time series of the equivalent velocity (Figure 9a) and PG term (see Figure 9b) were estimated for sites O1 and N9. The linear bottom drag coefficient (r) value was obtained by regression analysis where the measured depth averaged velocity ($\overline{v}_o$) at each site was regressed against the bottom stress values derived using the *Styles and Glenn* [2000] model (see section 4). The estimated PG time series (Figure 9b) is always directed opposite to the local alongshore wind forcing (Figure 9b). These results suggest that the estimated pressure gradient could potentially be the response to the wind forcing that was missing from our analysis, although further verification is needed.

[44] The south side of the study area is part of Raleigh Bay, a cuspate foreland system very similar in geometry and orientation as Onslow and Long Bays that are located farther south (see Figure 10a). Assuming a coherent wind system (vector correlation of winds measured at Diamond Shoals to Cape Lookout and Frying Pan Shoals is 1.81 and 1.60, respectively), the pressure gradients developed in between these bays must be of similar magnitude and orientation. Using this analogy, three months of subtidal pressure gradients term ($-g\partial\eta/\partial y$) calculated from the sea surface records of two tide gauges in Onslow Bay (Beaufort, NC and Wrightsville Beach, NC, see Figure 10a) is compared to the subtidal wind stress from the NOAA buoy at Frying Pan Shoals. The estimated PG term from Raleigh Bay (Figure 10b) shows similar variability as the wind stress component parallel to large scale shoreline ($\sim 60^\circ$ clockwise North, see Figure 10a) with a correlation coefficient (r) of -0.84. When the winds are directed toward the northeast, the PG term is negative suggesting the potential of flow toward the southwest, (i.e., opposite to direction of the wind), especially during relaxation periods. Furthermore, the magnitude of this term (Figure 10b) is of the same order (Figure 9b) as that estimated using equations (7) to (9) supporting our hypothesis that this magnitude of pressure gradient is required to close the momentum balance on the south side.

[45] In a similar manner, the generation of pressure gradient on the east side of Cape Hatteras and farther away from the measurement location is examined using the subtidal sea surface elevation records from the two nearest

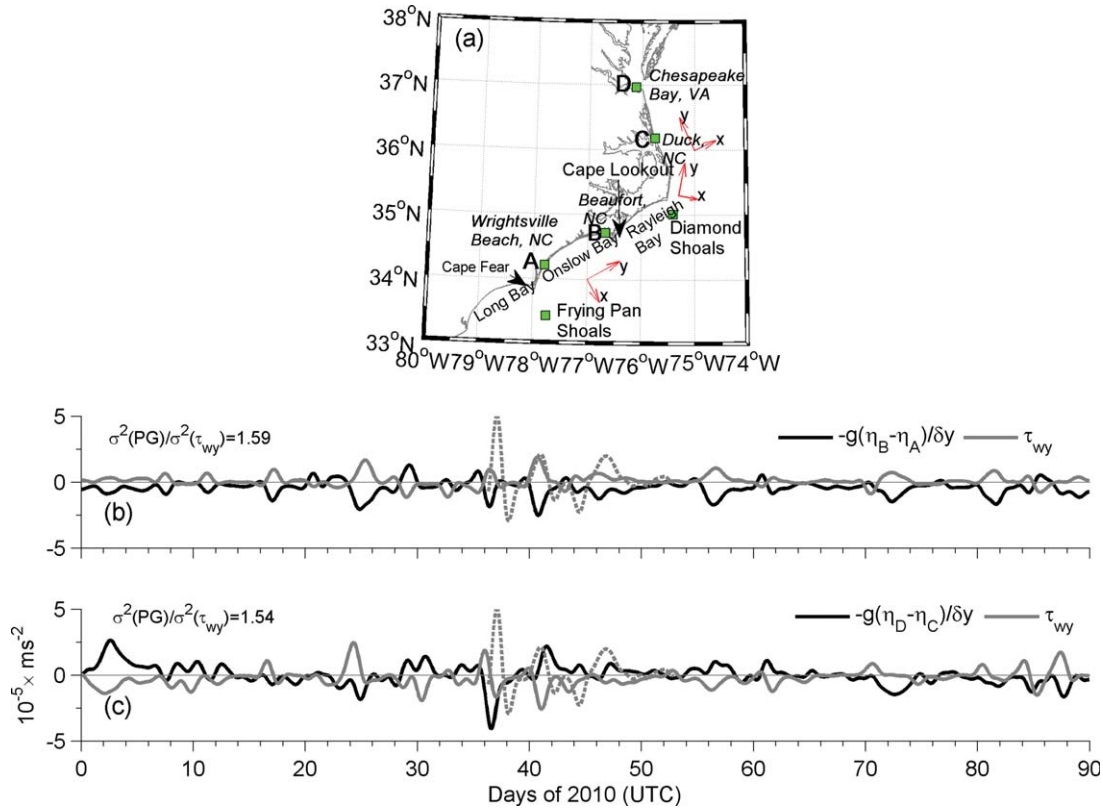

Figure 10. (a) Map of the South and Mid-Atlantic Bight showing the cuspate shapes of coastlines from Long Bay, (SC) to Cape Hatteras point (NC). The locations of NOAA tide gauges used to estimate pressure gradients are shown as squares. The three different coordinate systems used for determining local alongshore and cross-shore components of wind velocity for different regions of the coastline are shown in red. (b) Time series of low-pass filtered pressure gradient term, $-g\partial\eta/dy$ (black) between Wrightsville Beach (location A) and Beaufort, NC (location B), and low-pass filtered alongshore (gray) wind velocity from Frying Pan Shoals, (c) same as in Figure 10b but the pressure gradient is estimated between Duck, NC (location C) and Chesapeake Bay, VA (location D), and the along coastline wind velocity is estimated using the local coastline orientation between the tide gauges. Dashed gray line is Figure 10b and Figure 10c is the predicted pressure gradient term from equation (9) for the south side of Cape Hatteras.

oceanic tide gauges located in Chesapeake Bay, VA and Duck, NC (Figure 10a). The pressure gradient is again compared to the same wind forcing, with the alongshore component being appropriately defined using the shoreline orientation (~25°N counterclockwise from North, see Figure 10a) at this region. The PG term (Figure 10c) is of the same order of magnitude as that obtained on the south side and it is strongly correlated to local alongshore wind stress ($r = -0.68$). A more appropriate comparison of the response (i.e., pressure gradients) to forcing (i.e., alongshelf wind stress) for the two different locations requires normalization of the terms. The ratio of variances of the local (i.e., per side) subtidal alongshore wind stress and that of the pressure gradients from each side (σ^2(PG)/$\sigma^2(\tau_{wy})$) provides such a normalization and as we can see in Figures 10b and 10c the ratios are almost identical (1.59 and 1.54 for the remote south and east sides, respectively) implying the generation of the same pressure gradient for the same magnitude of alongshelf wind stress.

[46] The analysis presented above suggests that the pressure gradient acting as a response to alongshore wind forcing within the cuspate embayment on the south side is of the same order as that observed for the straight coastline on the remote east side. Nonetheless, unlike the south side, the momentum balance analysis on the near-field east side (i.e., at sites O2, N5, and N6, in the vicinity of the cape) is almost closed without the need for inclusion of pressure gradient. Upon closer examination, we note that the near-field, local coastline orientation of this area (i.e., from Duck, NC to Cape Hatteras, NC; Figure 10a) is different (larger) than that of the remote straight coastline farther east (i.e., from Chesapeake Bay, VA to Duck, NC; Figure 10a). The relative difference in coastline orientation between these two parts of the coastline is approximately 35°. This change in coastline orientation can lead to significant differences in the local alongshelf component of wind stress which might explain the lack of pressure gradient contribution on the east side of the study area. This analogue is similar to that presented by *Crépon and Richez* [1982] and *Crépon et al.* [1984] for transient upwelling generated by wind forcing and variability in the coastline. At this point, we should note that there is a small possibility that the pressure gradient estimated on the east side (Figure 10c) is partially balanced by the nonlinear advective

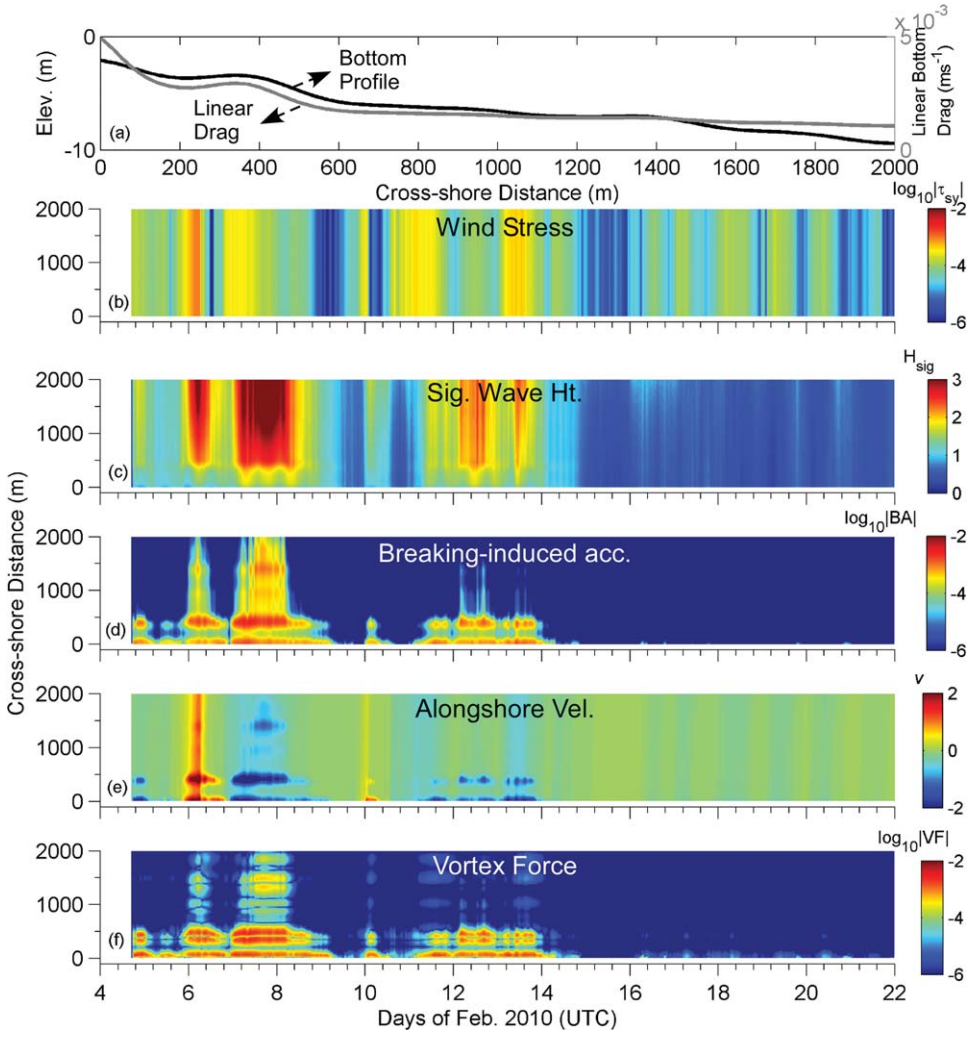

Figure 11. Cross-shore distribution of (a) linear bottom drag coefficient (black) and water depth (gray), color shading of (b) absolute value of wind stress ($m^2\ s^{-2}$), (c) significant wave height (m), (d) absolute value of breaking-induced acceleration ($m^2\ s^{-2}$), (e) alongshore current ($m\ s^{-1}$), and (f) vortex force ($m^2\ s^{-2}$) showing spatial (along *y* axis) and temporal (along *x* axis) variation. Log scale is used for Figures 11b, 11d, and 11f.

acceleration (see equation (1)) which was not included in this study, something that we cannot verify with our data at present. Additional field observations or numerical modeling is required to further investigate this issue.

5.2. The Role of Vortex Force

[47] The observations presented in section 4 provide some evidence regarding the importance of the VF and nonlinear advective acceleration terms in the alongshore momentum balance. This is further explored in here using a wave propagation model forced with the observed wind stress.

[48] The wave propagation model Simulating WAves Nearshore [SWAN, *Booij et al*., 1999] was set up on an alongshore uniform bathymetric domain with a bathymetry similar to that observed on the profile that passes through sites N5 and N6 (Figure 11a). The model was driven with the measured wind stress, sea surface variability, and offshore directional wave characteristics (height, peak period, mean direction, and directional spreading) as measured at Site O2. The results (i.e., cross-shore distribution of wave height, period, wave length, direction, and depth-limited dissipation) were then used to determine the breaking-induced acceleration term (see equation (5)).

[49] Considering only alongshore wind stress and breaking-induced accelerations as the forcing terms, and a cross-shore variable linear drag (Figure 11a), equation (6) is solved to obtain the cross-shore and temporal variability of the alongshore velocity. In this analysis, NA and VF terms are not accounted for and it is expected that the velocity structure obtained might differ from the measurements, especially during periods when the NA and VF terms were found to be important in the momentum balance analysis (section 4). The cross-shore component of Stokes drift is obtained from the SWAN derived wave conditions using equation (3), while the VF is determined as the product of Stokes drift and the cross-shore gradient of depth-averaged alongshore velocity.

[50] The velocity predicted using equation (6) (Figure 11e) shows similar variability and magnitude to that observed at

sites O2, N5, and N6, thus providing some confidence in this simplified analysis. The estimated breaking-induced acceleration becomes significant during the periods corresponding to the passage of the front systems (events F1 and F2), and the swell events S1 and S2 (Figure 11d). During these wave-dominated events, cross-shore variability in breaking-induced acceleration is present due to depth-limited breaking that occurs over the shallow areas of the nearshore bar. This is followed by a region of limited wave breaking and subsequently wave breaking commences again in shallower water depths. It is further established that in deeper water the magnitude of breaking-induced acceleration forcing is of the same order as that of wind stress and becomes more important with decreasing water depth. The variability of the modeled breaking-induced acceleration resembles that calculated from the measurements. In deeper waters ($\sim$10 m, e.g., site O2), wave breaking-induced acceleration is not present and wind stress is the dominant term, while in shallower waters (e.g., sites N5 and N6), breaking-induced acceleration is an order of magnitude higher than wind stress.

[51] The modeled VF estimates (Figure 11f) are important at all instances when wave breaking occurs, as this forcing mechanism leads to the formation of a cross-shore gradient in the alongshore velocity and thus an increase of horizontal shear ($\partial v/\partial x$). The cross-shore variability of VF is similar to that of breaking-induced acceleration and alongshore velocity, however, at locations with local maxima in alongshore velocity the VF term becomes zero ($\partial v/\partial x=0$). Maximum VF usually occurs around the bar and at locations with strongest cross-shore gradient in alongshore current. In deeper waters, VF (Figure 11f) is similar in magnitude to wind stress (Figure 11b).

[52] Overall, this simplified analysis suggests that in the transition zone between inner shelf and surf zone, even under moderate wave breaking, the role of VF term may be important and should be included. This might be particularly the case in locations where the alongshore component of the wind stress is reduced so that alongshore pressure gradients due to wind might not be as important as it appears to be the case for the near-field, east side of Cape Hatteras. Inside the surf zone, the balance can be more complex than traditionally described and the breaking-induced acceleration can be balanced by the sum of bottom stress, nonlinear acceleration, and VF, something also shown numerically using wave-current interaction 3-D models [*Kumar et al*., 2012; *Uchiyama et al*., 2010]. The transition (shoaling) zone between inner shelf and surf zone is an area that has not been thoroughly investigated at subtidal time scales. Our results indicate that in this region depending on the bathymetry, VF might be as important as bottom stress and wind stress.

[53] We should emphasize that the estimates of both VF and nonlinear advective acceleration presented in here are the results of a simple model. Since the time series length and cross-shore instrumentation density does not allow us to further evaluate the importance of our findings; a longer experiment with higher spatial resolution is recommended to address these issues.

6. Summary and Conclusions

[54] We presented wave and subtidal circulation data collected within the surf and inner shelf regions around the Cape Hatteras point, North Carolina, an area with complex morphology and abruptly changing shoreline orientation. Despite the short length of the time series, the winter season events identified and analyzed in here represent typical synoptic weather fronts in the South Atlantic Bight [e.g., *Austin and Lentz*, 1999; *Warner et al*., 2012], which is dominated by strong wind and wave forcing along with well mixed conditions. An important aspect of our work is the inclusion of Stokes-Coriolis (physically representing the influence of Earth's rotation on surface gravity waves) and vortex force (interaction between wave-induced mass drift and the mean flow vorticity) terms in the momentum balance analysis.

[55] Our analysis has shown that mean subtidal flows are parallel to the local coastline orientation on either side of the Cape Hatteras point, while in Diamond shoals the flows are directed along the shoal, suggesting that the shoal possibly acts as an extension of the coastline, regulating flow between the east and the south side of the cape. We believe these results are applicable to all coastlines with similar geometries (e.g., Cape Lookout, NC and Cape Fear, NC) in the South Atlantic Bight.

[56] In the absence of wind stress (i.e., swell-dominated events), the Stokes-Coriolis term is as important as Coriolis acceleration term, as was also shown in *Lentz* [2008] and it should not be neglected. Only under wind forcing when only locally generated, gravity waves are present and in the absence of swell forcing, Coriolis acceleration becomes the dominant term relative to Stokes-Coriolis term (also see *Fewings and Lentz*, 2010].

[57] Under spatially uniform wind forcing, changes in coastline orientation can lead to changes in alongshore pressure gradient due to changes in the alongshore component of the uniform wind field. It is hypothesized that this is the reason that allowed us to close the momentum balance on the south side of Cape Hatteras (section 5.1). The magnitude of this pressure gradient is contingent upon the relative angle of local coastline to the wind velocity vector. It can be further argued that for a constant wind field, the effect of coastline orientation in nearshore subtidal flows can be explained using an analogue of a spatially varying alongshelf wind stress even at scales of few kilometers (i.e., similar to *Crépon and Richez* [1982]).

[58] In shallower waters, the momentum balance is complex and a balance is achieved between bottom stress, breaking-induced acceleration, nonlinear advection, and vortex forces, as it has been also shown in three-dimensional modeling studies [*Uchiyama et al*., 2010; *Kumar et al*., 2012]. In the transition zone between inner shelf and surf zone, in the presence of strong along/cross-shore shear, the vortex force term can be of the same order as the wind stress, suggesting a need to include the former term in any study dealing with the flows and exchange between surf zone and inner shelf.

[59] Despite the limitations, the available data have been evaluated to the depths possible to identify the significant processes responsible for flow conditions around the Cape Hatteras point. This work has provided important glimpses into the role of coastline orientation in the development of subtidal circulation under wind and wave forcing. However, the coupling of observational data and numerical models can lead to better understanding of the

hydrodynamic processes including the effect of Vortex and Stokes-Coriolis force.

[60] **Acknowledgments.** The experimental work was funded by the Carolinas Coastal Processes Project, a cooperative study supported by the US Geological Survey. We thank U.S. Geological Survey personnel J. Borden, B. Armstrong, and M. Martini, involved in deployment of in situ acoustic sensors and postprocessing of data. Additional support during data analysis and preparation of this manuscript was provided by the National Science Foundation (award: OCE-1132130). N.K. also thanks Falk Feddersen and three anonymous reviewers for comments and suggestions, which substantially improved the manuscript.

References

Austin, J. A., and S. J. Lentz (1999), The relationship between synoptic weather systems and meteorological forcing on the North Carolina inner shelf, *J. Geophys. Res.*, *104*, 18,159 –18,185.

Barth, J. A., S. D. Pierce, and R. M. Castelao (2005), Time-dependent, wind-driven flow over a shallow midshelf submarine bank, *J. Geophys. Res.*, *110*, C10S05, doi:10.1029/2004JC002761.

Beardsley, R. C., R. Limeburner, and L. K. Rosenfeld (1985), Introduction to the CODE-2 moored array and large-scale data report, in *CODE-2: Moored Array and Large-Scale Data Report, WHOI Tech. Rep. WHOI-85-35*, p. 234, Woods Hole Oceanographic Institution, Woods Hole, Mass.

Bishop, C. T., and M. A. Donelan (1987), Measuring Waves with Pressure Transducers, *J. Coastal Eng.*, *11*, 309–328.

Booij, N., R. C. Ris and L. H. Holthuijsen (1999), A third-generation wave model for coastal regions, Part I, Model description and validation, *J. Geophys. Res.*, *104*(C4), 7649–7666.

Chen, Y., R. T. Guza, and S. Elgar (1997), Modeling spectra of breaking surface waves in shallow water, *J. Geophys. Res.*, *102*, 25,035–25,046.

Craik, A. D. D., and S. Leibovich (1976), A rational model for Langmuir circulations, *J. Fluid Mech.*, *73*, 03, 401–426.

Church, J. C., and E. B. Thornton (1993), Effects of breaking wave induced turbulence within a longshore current model, *Coastal Eng.*, *20*, 1–28.

Crépon, M., and C. Richez (1982), Transient upwelling generated by two dimensional atmospheric forcing and variability in the coastline, *J. Phys. Oceanogr.*, *12*, 1437– 1457.

Crépon, M., C. Richez, and M. Chartier (1984), Effects of coastline geometry on upwellings, *J. Phys. Oceanogr.*, *14*, 1365–1382.

Crosby, D. S., L. C. Breaker, and W. H. Gemmill (1993), A proposed definition for vector correlation in geophysics: Theory and application, *J. Atmos. Oceanic Technol.*, *10*(3), 355–367.

Feddersen, F., R. T. Guza, S. Elgar, and T. H. C. Herbers (1998), Alongshore momentum balances in the nearshore, *J. Geophys. Res.*, *103*, 15,667–15,676.

Fewings, M. R. (2007), Cross-shelf circulation and momentum and heat balances over the inner continental shelf near Martha's Vineyard, Massachusetts, PhD thesis, 267 pp., Massachusetts Inst. of Technol., Cambridge. [Available at http://hdl.handle.net/1721.1/42066.]

Fewings, M. R., and S. J. Lentz (2010), Momentum balances on the inner continental shelf at Martha's Vineyard Coastal Observatory, *J. Geophys. Res.*, *115*, C12023, doi:10.1029/2009JC005578.

Gan, J., and J. S. Allen (2002a), A modeling study of the shelf circulation off northern California in the region of the Coastal Ocean Dynamics Experiment: 2. Simulations and comparisons with observations, *J. Geophys. Res.*, *107*(C11), 3184, doi:10.1029/2001JC001190.

Gan, J., and J. S. Allen (2002b), A modeling study of the shelf circulation off northern California in the region of the coastal ocean dynamics experiment: Response to relaxation of upwelling winds, *J. Geophys. Res.*, *107*(C9), 3123, doi:10.1029/2000JC000768.

Garrett, C. J. R., and Toulany, B. (1981), Variability of the flow through the Strait of Belle Isle, *J. Mar. Res.*, *39*, 163–189.

Gutierrez, B. T., G. Voulgaris, and P. A. Work (2005), Cross-shore variation of wind-driven flows on the inner shelf in Long Bay, South Carolina, United States, *J. Geophys. Res.*, *111*, C03015, doi:10.1029/2005JC003121.

Hasselmann, K. (1970), Wave-driven inertial oscillations, *Geophys. Fluid Dyn.*, *1*, 463–502.

Herbers, T. H. C., E. J. Hendrickson, and W. C. O'Reilly (2000), Propagation of swell across a wide continental shelf, *J. Geophys. Res.*, *105*(C8), 19,729–19,737, doi:10.1029/2000JC900085.

Herbers, T. H. C., S. Elgar, and R.T. Guza (1999), Directional spreading of waves in the nearshore, *J. Geophys. Res.*, *104*(C4), 7683–7693.

Kirincich, A. R., and J. A. Barth (2009), Along-shelf variability of inner-shelf circulation along the central Oregon coast during summer, *J. Phys. Oceanogr.*, *39*, 1380–1398.

Krystek, M., and M. Anton (2007), A weighted total least-squares algorithm for fitting a straight line, *Meas. Sci. Technol.*, *18*, 3438–3442.

Kumar, N., G. Voulgaris, J. C. Warner, and M. Olabarrieta (2012), Implementation of the vortex force formalism in the coupled ocean-atmosphere-wave-sediment transport (COAWST) modeling system for inner shelf and surf zone applications, *Ocean Modell.*, *47*, 65–95.

Large, W. G., and S. Pond (1981). Open ocean momentum flux measurements in moderate to strong winds, *J. Phys. Oceanogr.*, *11*, 324–336.

List, J. H., J. C. Warner, E. R. Thieler, K. Haas, G. Voulgaris, J. E. McNinch, and K. L. Brodie (2011), A nearshore processes field experiment at Cape Hatteras, North Carolina, USA, in *Proceedings of the Coastal Sediments*, edited by Julie D. Rosati, Ping Wang and Tiffany M. Roberts, pp. 2144–2157, World Scientific, Singapore.

Lentz, S. J. (1994), Current dynamics on the northern California inner shelf, *J. Phys. Oceanogr.*, *24*, 2461–2478.

Lentz, S. J. (2001), The influence of stratification on the wind-driven cross-shelf circulation over the North Carolina Shelf. *J. Phys. Oceanogr.*, *31*, 2749–2760.

Lentz, S. J. (2008), Observations and a model of the mean circulation over the Middle Atlantic Bight continental shelf, *J. Phys. Oceanogr.*, *38*, 1203–1221.

Lentz, S. J., and M. R. Fewings (2012), The wind-and wave-driven inner-shelf circulation. *Annu. Rev. Mar. Sci.*, *4*, 317–343, doi: 10.1146/annurev-marine-120709–142745.

Lentz, S. J., and C. D. Winant (1986), Subinertial currents on the southern California shelf, *J. Phys. Oceanogr.*, *16*, 1737–1750.

Lentz, S., R. T. Guza, S. Elgar, F. Feddersen, and T. H. C. Herbers (1999), Momentum balances on the North Carolina inner shelf, *J. Geophys. Res.*, *104*, 18,205–18,226.

McNinch, J. E., and R. A. Luettich Jr. (2000), Physical processes around a cuspate foreland headland: Implications to the evolution and long-term maintenance of a cape-associated shoal, *Cont. Shelf Res.*, *20*(17), 2367–2389.

Roughan, M., A. J. Mace, J. L. Largier, S. G. Morgan, J. L. Fisher, and M. L. Carter (2005), Subsurface recirculation and larval retention in the lee of a small headland: A variation on the upwelling shadow theme, *J. Geophys. Res.*, *110*, C10027, doi:10.1029/2005JC002898.

Sanay R., G. Voulgaris, and J. C. Warner (2007), Influence of tidal asymmetry and residual circulation on sediment transport in linear sandbanks: A processes-oriented numerical study, *J. Geophys. Res.*, *112*, C12015, doi: 10.1029/2007JC004101.

Styles, R., and S. M. Glenn (2000), Modeling stratified wave and current bottom boundary layers on the continental shelf, *J. Geophys. Res.*, *105*(C10), 24,119–24,139, doi:10.1029/2000JC900115.

Uchiyama, Y., J. C. McWilliams, and A. F. Shchepetkin (2010), Wave-current interaction in an oceanic circulation model with a vortex force formalism: Application to the surf zone, *Ocean Modell.*, *34*(1–2), 16–35.

Warner, J. C., Armstrong, B., Sylvester, C. S., Voulgaris, G., Nelson, T., Schwab, W. C., and J. F. Denny (2012), Storm-induced inner-continental shelf circulation and sediment transport: Long Bay, South Carolina, *Cont. Shelf Res. 42*, 51–63.

Welch, P. D. (1967), The use of fast Fourier transform for the estimation of power spectra: A method based on time averaging over short, modified periodograms, *IEEE Trans. Audio Electr.*, *15*, 70–73.